

# Antiferromagnetic resonance in $\alpha\text{-Fe}_2\text{O}_3$ up to its Néel temperature

M. Bialek,<sup>1, a)</sup> J. Zhang,<sup>2</sup> H. Yu,<sup>2, 3</sup> and J.-Ph. Ansermet<sup>1, 3</sup>

<sup>1)</sup>*Institute of Physics, École Polytechnique Fédérale de Lausanne (EPFL), 1015 Lausanne, Switzerland*

<sup>2)</sup>*Fert Beijing Institute, MIT Key Laboratory of Spintronics, School of Integrated Circuit Science and Engineering, Beihang University, Beijing, China*

<sup>3)</sup>*International Quantum Academy, Shenzhen 518048, China*

(Dated: 12 July 2022)

Hematite ( $\alpha\text{-Fe}_2\text{O}_3$ ) is an antiferromagnetic material with a very low spin damping and high Néel temperature. The temperature dependence of the antiferromagnetic resonance in a bulk single crystal of hematite was characterized from room temperature up to the Néel temperature in the frequency range of 0.19–0.5 THz. From these data, the Néel temperature was estimated as 966 K.

Hematite ( $\alpha\text{-Fe}_2\text{O}_3$ ) is a very common room-temperature antiferromagnet of the Néel temperature, reported as  $T_N = 946$  K,<sup>1</sup>  $T_N = 950$  K,<sup>2</sup>  $953$  K,<sup>3</sup>  $960$  K,<sup>4</sup>  $972$  K.<sup>5</sup> It is characterized by a very low spin damping that make it promising for spintronic applications<sup>6–11</sup> and strong light-matter coupling.<sup>12,13</sup> Above the spin-reorientation transition (Morin phase transition) at about  $T_M = 260$  K,<sup>2,14</sup> the superexchange Dzialoshinskii-Moriya interaction leads to canting of the two sublattices that gives rise to net magnetisation  $\mathbf{m}$ , i.e. making this material a weak ferromagnet.

Hematite crystallizes in an approximately hexagonal structure with space group  $R\bar{3}c$ . Precise measurements show that the actual symmetry is monoclinic  $C2/c$ <sup>15</sup>. In the weak ferromagnetic state the ferromagnetic moment  $\mathbf{m}$  is along  $a$  axis<sup>16,17</sup> (magnetic symmetry  $C2'/c$ <sup>15</sup>) or  $b$  axis<sup>2,16</sup> (magnetic symmetry  $C2/c$ )<sup>1,15</sup>. Owing to the spin canting, the antiferromagnetic resonance has two modes: at a higher frequency, the quasi-antiferromagnetic resonance (qAFMR) mode which is excited when the dynamical magnetic field  $\mathbf{h}$  is parallel to the magnetization ( $\mathbf{h} \parallel \mathbf{m}$ ), and at low frequencies, the quasiferromagnetic resonance (qFMR) mode, excited by a dynamical magnetic field perpendicular to the magnetization ( $\mathbf{h} \perp \mathbf{m}$ ). In this work, we characterize the qAFMR mode up to the Néel temperature, which was observed previously up to about 600 K<sup>2</sup> and below room temperature<sup>14</sup>.

The qFMR mode has non-zero frequency only with external field applied<sup>18,19</sup> and falls below our experimental range. To our knowledge, the qFMR mode was investigated only at room temperature and below<sup>20–22</sup>.

Development of frequency extenders for vector network analyzers (VNA) allows continuous-wave spectroscopic measurements up to 1.5 THz to be conducted with a high frequency resolution and with a very high dynamic range<sup>12,23–26</sup>. Our sample was a natural single crystal of  $\alpha\text{-Fe}_2\text{O}_3$  of  $d = 0.5$  mm in thickness and  $10 \times 10$  mm<sup>2</sup> in lateral dimensions. The normal to the sample surface was (11-20).

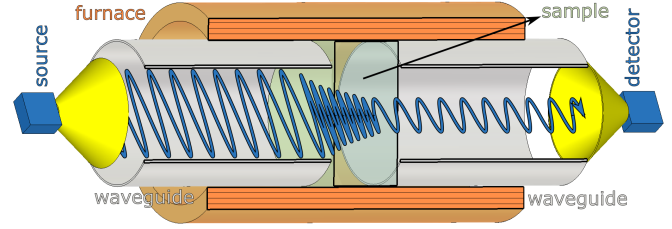


FIG. 1. Schematic of the THz spectrometer (not to scale): source and detector VNA extenders, horns, oversized waveguides, the sample is heated with a furnace.

Figure 1 shows a schematic of our THz setup, where terahertz radiation generated by the source extender was guided to the sample using oversized metallic waveguides. Transmitted radiation was guided from the sample to the detector using identical oversized metallic waveguides. Detector measured incoming power and phase of the electric field. Temperature scans started from the highest temperature with a step of  $\Delta T = -0.25$  K. We chose  $\Delta T$  so that change of the resonance frequency with temperature is smaller than the line width of the resonance, which is particularly narrow at lower temperatures. After stabilizing sample temperature  $T$  with a PID controller, we measured transmission as a function of radiation frequency  $f$ . The recorded spectra were obtained by averaging 20 frequency sweeps measured with 100 Hz bandwidth of extenders intermediate frequency bandwidth. This procedure was applied at two frequency bands of 0.19–0.35 THz and 0.33–0.5 THz using different sets of frequency-extendors. We recorded relative transmitted radiation power in  $dB$  and the phase of the transmitted electric field in  $deg$  units. This way, a complex transmission data matrix  $S_{21}(f, T)$  was obtained.

The source extender emits linearly polarized beam of THz radiation and the detector extender detects only radiation of a linear polarization that matches its waveguide. Rotation of the polarization plane about the optical axis is possible by rotating the source and detector about the optical axis. The data presented here, were obtained with parallel source and detector polarizations.

Raw spectra are dominated by interference occurring

<sup>a)</sup>Electronic mail: marcin.bialek@fuw.edu.pl

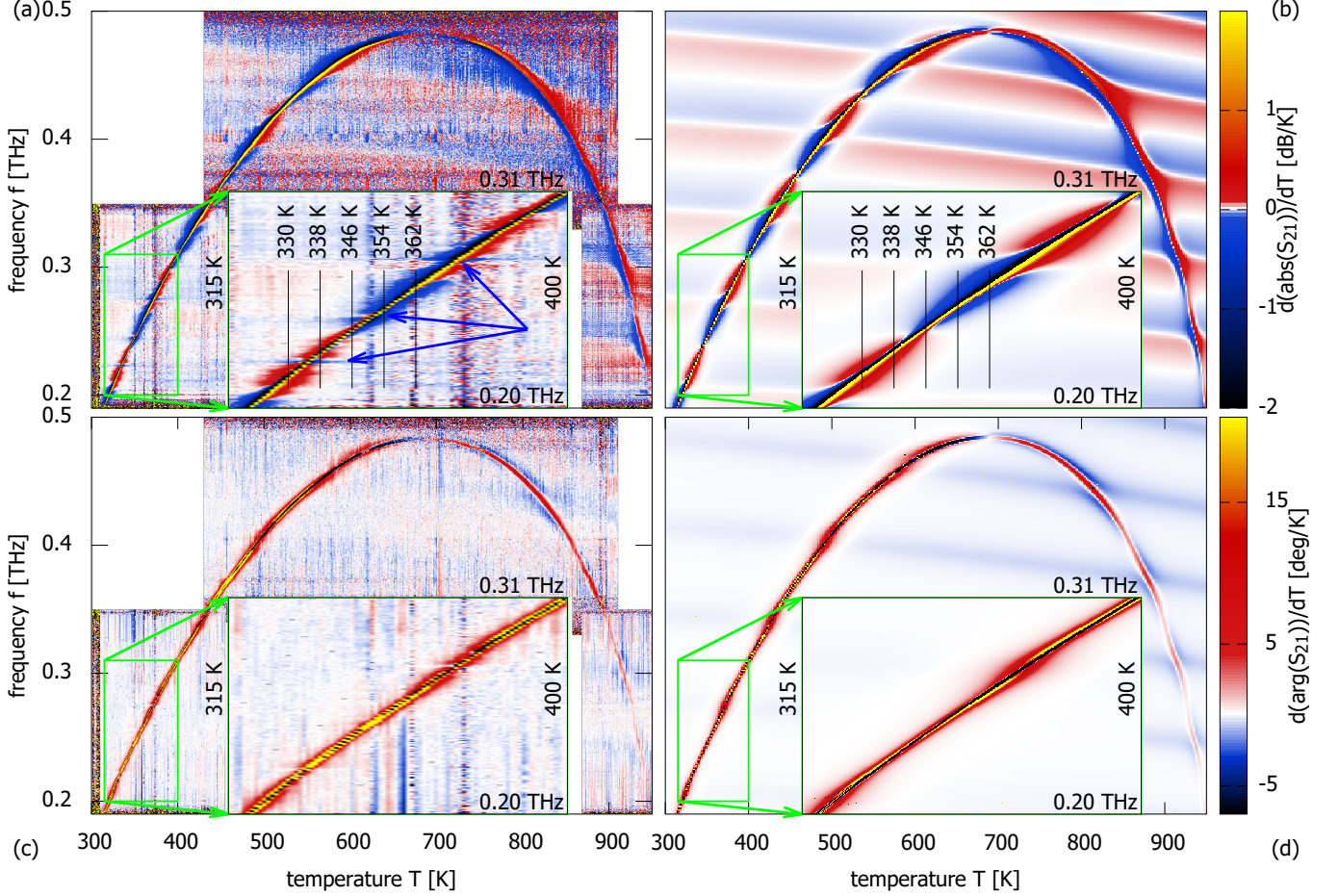


FIG. 2. Temperature-differential transmission through a bulk crystal, magnitude (a) and phase (c) data. Fit of the global model: magnitude (b) and phase (d) using Eq. 3–9 with parameters from Tab. I. Insets : zoom on a narrow temperature window, temperature marks in (a) and (b) are those of the line plots in Fig. 4. Blue arrows point to stronger interaction with cavity modes of the setup.

between components of the experimental setup. Since this pattern very weakly depends on temperature, we eliminated it by calculating temperature-derivative spectra, that is, by subtracting successive spectra from one another. We calculated magnitude temperature-derivative spectra

$$\frac{d|S_{21}|}{dT} = \frac{|S_{21}(f, T + \Delta T)| - |S_{21}(f, T)|}{\Delta T}, \quad (1)$$

and phase derivative:

$$\frac{d(\arg S_{21})}{dT} = \frac{\arg(S_{21}(f, T + \Delta T)) - \arg(S_{21}(f, T))}{\Delta T}. \quad (2)$$

Our main results are presented in Fig. 2a (magnitude) and Fig. 2c (phase). They were obtained with the THz magnetic field acting in the basal plane of the crystal, as determined from polarization-dependent results in Fig. 3. At a perpendicular polarization, with THz magnetic field along  $c$  axis, the resonance is almost not excited. We can notice the the resonance peak shows a tiny splitting

of about 1 GHz. Result of angular dependence obtained with a  $c$ -cut sample shows a more complex dependence on polarization angle that is different for a higher and a lower modes of the qAFMR (green circles and blue rectangles in Fig. 3b). This angular dependence suggests that the observed splitting is related to different magnetic domains in our samples.

We observed a strong and narrow resonance (Fig. 2b and c), the frequency of which is rising with temperature at above room temperature (Fig. 2a), reaching a maximum of about 484 GHz at about 685 K and then dropping sharply as  $T_N$  is approached. The periodic, almost horizontal pattern is related to the Fabry-Pérot type cavity modes inside the sample. We can account for these temperature-differential spectra, as shown in Fig. 2 (b, d), by using an electrodynamics-based model<sup>26</sup>:

$$\frac{d|S_{21}(f, T)|}{dT} = \frac{20}{\Delta T} \log_{10} \frac{|t(f, T + \Delta T)|}{|t(f, T)|}, \quad (3)$$

where  $t$  is the transmittance of a plane electromagnetic

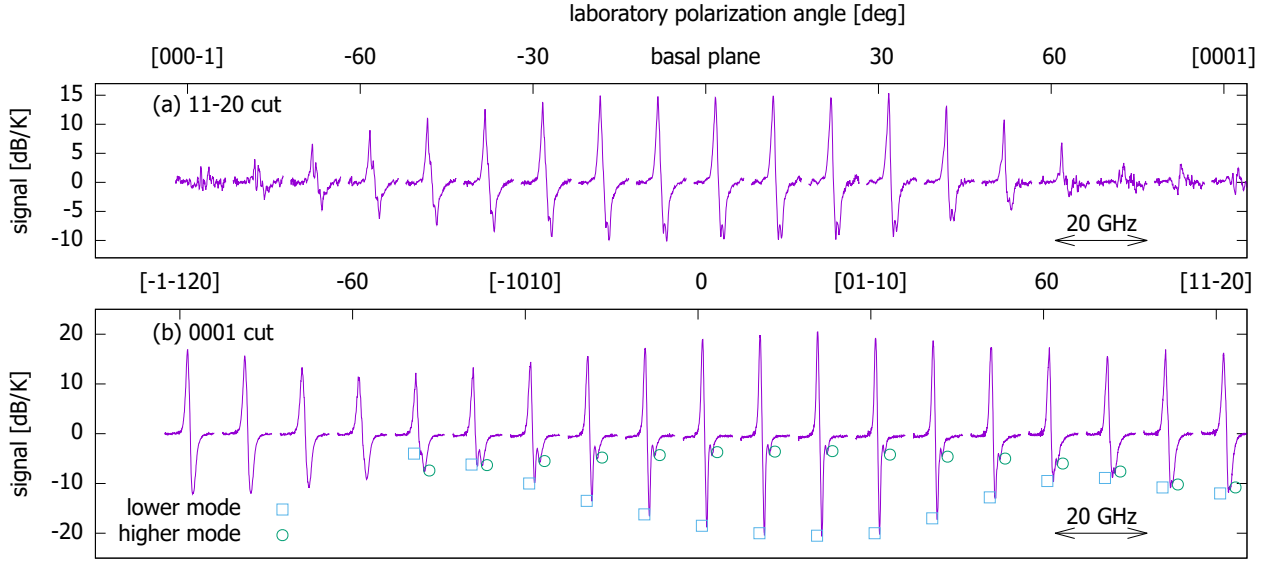


FIG. 3. Temperature-differential spectra near the resonance measured at different polarization angles for (a) 11-20 cut sample at 324.0 K and for (b) 0001 cut sample at 321.5 K. Spectra are shifted for clarity to show dependence of the resonance magnitude on polarization angle. In (a), for  $\alpha = 0^\circ$ , THz magnetic field is in the basal plane and for  $|\alpha| = 90^\circ$  it is along  $c$  axis. In (b), the points are guide for the eye, highlighting the amplitudes of qAFMR lower and higher modes.

wave at normal-incident on a parallel-plane slab of infinite lateral dimensions and thickness  $d$

$$t = \frac{(1 - r^2)e^{ikd}}{1 - r^2e^{2ikd}}. \quad (4)$$

Here,  $r = (\sqrt{\epsilon} - \sqrt{\mu})/(\sqrt{\epsilon} + \sqrt{\mu})$  and  $k = 2\pi f\sqrt{\epsilon\mu}/c$ . We assume an isotropic slab material characterized by its permeability  $\mu(f, T)$  and permittivity  $\epsilon(f, T)$ . Our crystal is not isotropic, but in the case of incidence at a normal angle to the crystal surface, the crystal being cut in one of its principal axis, we approximate it as isotropic, that is, we assume that there is no rotation of polarization in the crystal. At other angles of incident beam polarization, we get different values of  $\epsilon$ . However, as long as we were interested in the behaviour of the antiferromagnetic resonance, we determined permittivity at the polarization angle where the resonance is excited the strongest. Since this occurs when the dynamical magnetic field is in the basal plane, the  $\epsilon$  that we determined in this communication describes response of hematite when exposed to dynamical electric field acting in the  $c$  axis.

The assumptions made for both  $\mu$  and  $\epsilon$  are the following. We found that our data are sensitive to a temperature dependence of the dielectric response function. The simplest model that accounts for our data is a real second order polynomial of temperature. This approximation is justified because our frequency range is far from optical phonons (the lowest at about 7.5 THz)<sup>27-29</sup> and dielectric absorption is negligible. Thus, we assumed

$$\epsilon = \epsilon_{900} + a(T - T_0) + b(T - T_0)^2, \quad (5)$$

where  $T_0 = 900$  K,  $\epsilon_{900} = 23.405$ ,  $a = 1.139 \cdot 10^{-2} K^{-1}$ ,

$b = 6.434 \cdot 10^{-6} K^{-2}$ . To account for the magnetic resonance, we assumed that the permeability has the form of two Lorentzian functions to account for the observed splitting of the qAFMR mode

$$\mu = 1 + \frac{\Delta\mu_1 f_r^2}{f_r^2 - f^2 - ifg_1} + \frac{\Delta\mu_2 (f_r + \Delta f)^2}{(f_r + \Delta f)^2 - f^2 - ifg_2}. \quad (6)$$

Here,  $\Delta\mu_1 + \Delta\mu_2 = \Delta\mu$  gives the total static magnetic susceptibility,  $f_r$  is the lower qAFMR frequency,  $g_1$  and  $g_2$  are widths of the two split resonances and  $\Delta f$  is the splitting of about 1 GHz. In the next paragraphs we describe these parameters.

In order to describe the temperature dependence of the antiferromagnetic resonance, we first fitted the resonance frequency, amplitude, and line widths in temperature intervals of 2 K around some temperature  $T_0^{(l)}$ , where  $l$  is the interval number. Within each such interval, we put amplitudes and widths independent of temperature and we fit the resonance frequency with a first order polynomial  $f(T)^{(l)} = f_{T_0}^{(l)} + f_T^{(l)}(T - T_0)$ . Results of these temperature interval fittings are shown as green crosses in Fig. 2(a,b,c). We show in Fig. 4(a) middle frequency  $f_{T_0}^{(l)}$  obtained in given temperature interval.

These results allowed us to assume some simple functional dependences that are approximately valid in the entire experimental temperature range. The global fitting result, using the above assumptions, are displayed in Fig. 2(b) and (d). The fit parameter values are given in Tab. I. The functions used to describe modes frequencies, amplitudes and widths are drawn as solid yellow lines in Fig. 4.



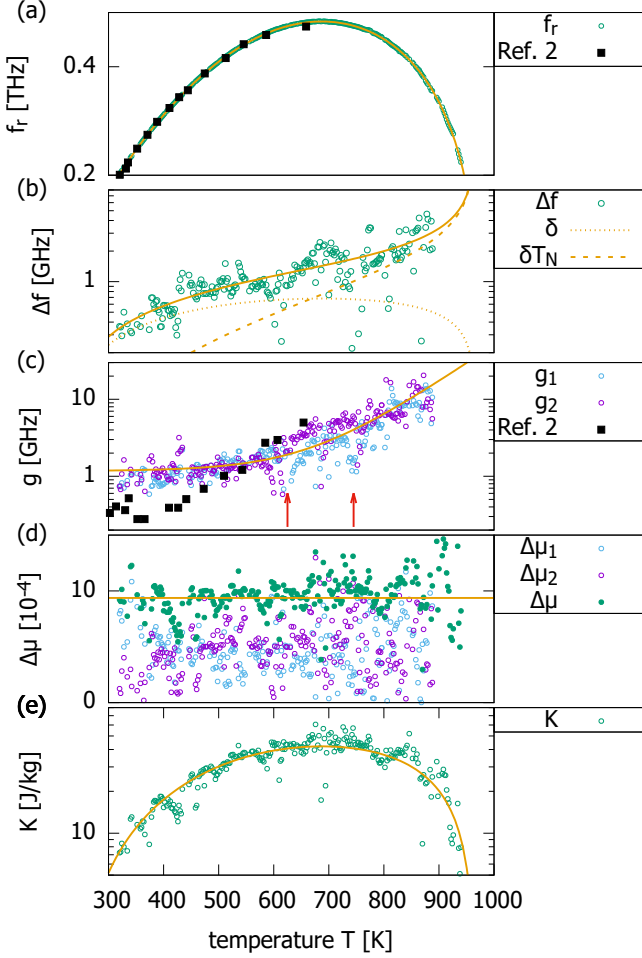


FIG. 4. Temperature dependence of the resonance frequency  $f_r$  (a), amplitude  $\Delta\mu_1$  and  $\Delta\mu_2$  (b), width  $g_1$  and  $g_2$  (c), frequency splitting  $\Delta f$  (d), and magnetic anisotropy factor  $K$  (e). Points come from 2 K intervals fits. The solid lines are calculated using Eq. 7–10 with parameters from Tab. I. In (a) and (c), black rectangles come from Ref. 2.

$a_2$	$-3.2 \pm 0.3$	$\text{GHz}^2\text{K}^{-2}$
$a_3$	$1.836 \pm 0.017$	$10^{-2}\text{GHz}^2\text{K}^{-3}$
$a_4$	$-2.40 \pm 0.03$	$10^{-5}\text{GHz}^2\text{K}^{-4}$
$a_5$	$1.113 \pm 0.019$	$10^{-8}\text{GHz}^2\text{K}^{-5}$
$\beta$	$0.499 \pm 0.005$	
$T_N$	$965.9 \pm 0.4$	K
$\Delta\mu$	$9.4 \pm 0.24$	$10^{-4}$
$g_{400}$	$1.17 \pm 0.15$	GHz
$g_e$	$34 \pm 3$	GHz
$g_s$	$1.12 \pm 0.07$	$10^{-2}\text{K}^{-1}$
$\delta$	$1.41 \pm 0.11$	$10^{-3}$
$\delta T_N$	$1.21 \pm 0.06$	K

TABLE I. Obtained global fit parameters.

To describe the observed temperature dependence of the resonant frequency (Fig. 4a), we took the dependence of the resonant frequency to follow a modified power law<sup>30</sup>

$$f_r(T) = \sqrt{\sum_{j=2}^{j=5} a_j T^j} \left(1 - \frac{T}{T_N}\right)^\beta, \quad (7)$$

where  $T_N$  is a parameter close to the Néel temperature and the power factor  $\beta$  is expected to be about 1/2. We modified the classical power law adding a 5-th order polynomial that lets us heuristically describe its non-monotonic dependence on temperature. This non-monotonic dependence of resonance frequency on temperature is caused by the strong temperature dependence of the magnetic anisotropy field<sup>31</sup> that governs the frequency of this mode. It is related to the spin-reorientation transition at about 260 K<sup>2</sup>, with one of its effects being that the qAFMR mode frequency has a minimum at this temperature. The fit value of  $T_N \approx 966$  K is within the spread of literature values of  $T_N = (946 - 972)$  K<sup>1,3-5</sup>. These inconsistencies in the literature might stem from errors in temperature measurement in different experiments. However, it may be also due to different models used to determine  $T_N$ , when it is determined by extrapolation.

We assumed that the observed splitting (Fig. 4b) can be described in the following way

$$\Delta f = \delta f_r + f_r(T)_{T_N=T_N+\delta T_N/2} - f_r(T)_{T_N=T_N-\delta T_N/2}, \quad (8)$$

which express our expectation that the splitting is caused by presence of two types of domains characterized by slightly different anisotropy fields (factor  $\delta$ ) and slightly different critical temperatures (factor  $\delta T_N$ ). The second term dominates at high temperatures. Inhomogeneous nature of this splitting is justified by the measurements for 0001 cut sample (Fig. 3b) that show that upper and lower modes have different dependence on polarization angle. The observed temperature dependence of the splitting can be well fitted (Fig. 4b) with the Eq. 8 using reasonable values of  $\delta$  and  $\delta T_N$  (Tab. I).

Taking into account the scatter in Fig. 4d, we took amplitudes of the resonance  $\Delta\mu_1 = \Delta\mu_2 = \frac{1}{2}\Delta\mu$  to be independent of temperature. This scatter is probably due to imperfect interval fits, especially pronounced at around 700 K and close to  $T_N$ , owing to low signal obtained by temperature-differential transmission in these temperature ranges.

We assumed that the temperature dependence of the observed width (Fig. 4c) of both modes is described by the same function consisting of a sum of a constant and an exponential,

$$g(T) = g_{400} + g_e e^{g_s(T-T_N)}, \quad (9)$$

where the latter dominates close to  $T_N$ . It could be due to either: 1) temperature inhomogeneity, 2) inhomogen-

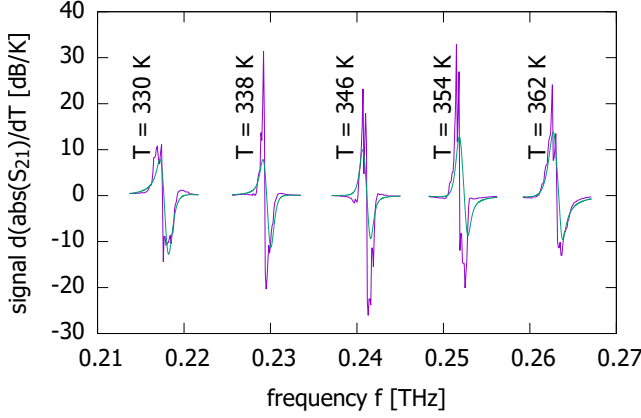


FIG. 5. Experimental spectra (purple) and the global fitting result (green) at selected temperatures, marked in insets of Fig. 2ab.

ity of  $T_N$ , 3) homogeneous line broadening. We can exclude the 1st possibility, as if it was the dominant mechanism, the linewidth would be proportional to  $|df_r/dT|$ , and we would see a drastic drop in the linewidth around 700 K, where  $df_r/dT = 0$ . For the 2nd possibility we can estimate the distribution of  $T_N$  that could cause such a broadening by solving  $f_r(T) \pm \frac{1}{2}g_e e^{g_s(T-T_N)} = \sqrt{\sum_{j=2}^{j=5} a_j T^j (1 - T/T_{N\pm})^\beta}$ . The maximum  $T_{N+} - T_{N-}$  that is necessary to account for the observed broadening is about 6 K, which is much larger than estimation of  $\delta T_N = 1.2$  K obtained from the splitting of the resonance. Therefore, we conclude that the observed broadening with temperature is mainly due to rising spin damping.

We notice that the linewidth drops strongly around 620 K and 740 K (two arrows in Fig. 4c). Since at these two temperatures, the frequency of the resonance is about 475 GHz, we can guess that this effect is due to interaction of the magnetic resonance with either some electromagnetic mode in the setup or some electric transition in the crystal that has a temperature-independent frequency.

There are features in Fig. 2 that are possibly caused by interaction with cavity modes than cannot be taken into account within our one-dimensional model. The effects of some of such modes are shown with blue arrows in the inset of Fig. 2a and a particular example of a lineshape distortion is shown in Fig. 5 at  $T = 346$  and 354 K. We can clearly see that, at different temperatures, the lineshape changes and some of these features are not reproduced by our global one-dimensional model. Blue arrows in Fig. 2a show that these are indeed related to modes of cavities that cannot be taken into account by the global model, which show-up as almost temperature-independent horizontal lines distorting the resonance in the inset of Fig. 2a that are not reproduced by the fit in inset of Fig. 2b. These distortions cause apparent fluctuations of width and amplitude of the resonance line in

the obtained temperature-interval fit values.

We observed weak interaction of magnetic resonance with electromagnetic standing waves, as found previously<sup>26</sup>. These effects are readily taken into account by a classical electrodynamic model. Light-matter interaction when the sample is its own cavity is in a weak regime, because the quality factor of modes of dielectric cavity is low. Nevertheless, these electromagnetic cavity modes already have a dramatic and nontrivial effect on the observed lineshapes, as shown in Fig. 4b and Fig. 4c.

In Fig. 4e we also included the magnetic anisotropy factor, which we deduced from equation  $K = \mu_0 H_A M_0$ , where  $H_A$  is anisotropy field and  $M_0$  is a saturation magnetisation of a sublattice. To do so, we took into account that the static magnetic susceptibility is given by  $\chi_\perp = M_0/2H_E$ , where  $H_E$  is exchange field, and that  $\chi_\perp = \Delta\mu_2/\rho_m$ , where  $\rho_m = 5.27 \cdot 10^3$  kg/m<sup>3</sup> is the hematite mass density<sup>32</sup>. Then, using the Kittel's equation

$$2\pi f_r = \gamma\mu_0 \sqrt{2H_E H_A} = \gamma \sqrt{\frac{K\mu_0}{\chi_\perp}}, \quad (10)$$

we found the mass density of the magnetic anisotropy energy. We see in Fig. 4e that  $K$  has a complex behaviour, which is known to be caused by the spin-reorientation transition that occurs at about 260 K.

Hematite single crystals present a very narrow resonance around room temperature, about 1 GHz. The resonance frequency increases sharply above room temperature and reaches a maximum of 484 GHz at about 685 K and then, the mode softens steeply when approaching the Néel temperature  $T_N$ . Above 690 K, the observed width of the resonance rises exponentially with temperature. Weak light-matter coupling was observed between the qAFMR mode and the standing waves inside the slab itself. The qAFMR mode presents a splitting that was ascribed to domains in the sample.

Support by the Sino-Swiss Science and Technology Cooperation (SSSTC) grant no. EG-CN.02.032019 is gratefully acknowledged. The VNA and frequency extenders were funded by EPFL and the SNF R'Equip under Grant No. 206021.144983.

The authors have no conflicts to disclose. The data that support the findings of this study are available from the corresponding author upon reasonable request.

<sup>1</sup>L. Oravova, Z. Zhang, N. Church, R. J. Harrison, Ch. J. Howard, and M. A. Carpenter. Corrigendum: Elastic and anelastic relaxations accompanying magnetic ordering and spin-flop transitions in hematite, Fe<sub>2</sub>O<sub>3</sub>. *Journal of Physics: Condensed Matter*, 25(25):259501, may 2013.

<sup>2</sup>K. S. Aleksandrov, L. N. Bezmaternykh, G. V. Kozlov, S. P. Lebedev, A. A. Mukhin, and A. S. Prokhorov. Anomalies of high-frequency magnetic permeability of hematite at the Morin phase transition. *Journal of Experimental and Theoretical Physics*, 65(3):591, 1986.

<sup>3</sup>F. J. Morin. Magnetic Susceptibility of  $\alpha$ -Fe<sub>2</sub>O<sub>3</sub> and  $\alpha$ -Fe<sub>2</sub>O<sub>3</sub> with Added Titanium. *Phys. Rev.*, 78:819–820, Jun 1950.

<sup>4</sup>N. B. Nešković, B. Babić, and J. Konstantinović. High temperature anomalous behaviour of the crystal lattice of hematite. *physica status solidi (a)*, 41(2):K133–K136, 1977.

- <sup>5</sup>K. Ono and A. Ito. A Mossbauer Study of the Internal Field at  $\text{Fe}^{57}$  in  $\alpha\text{-Fe}_2\text{O}_3$ . *Journal of the Physical Society of Japan*, 17(6):1012–1017, 1962.
- <sup>6</sup>O. R. Sulymenko, O. V. Prokopenko, V. S. Tiberkevich, A. N. Slavin, B. A. Ivanov, and R. S. Khymyn. Terahertz-frequency spin hall auto-oscillator based on a canted antiferromagnet. *Phys. Rev. Applied*, 8:064007, Dec 2017.
- <sup>7</sup>P. Stremoukhov, A. Safin, M. Logunov, S. Nikitov, and A. Kirilyuk. Spintronic terahertz-frequency nonlinear emitter based on the canted antiferromagnet-platinum bilayers. *Journal of Applied Physics*, 125(22):223903, 2019.
- <sup>8</sup>J. Fischer, M. Althammer, N. Vlietstra, H. Huebl, S. T.B. Goennenwein, R. Gross, S. Geprägs, and M. Opel. Large Spin Hall Magnetoresistance in Antiferromagnetic  $\alpha\text{-Fe}_2\text{O}_3/\text{Pt}$  Heterostructures. *Phys. Rev. Applied*, 13:014019, Jan 2020.
- <sup>9</sup>R. Lebrun, A. Ross, O. Gomonay, V. Baltz, U. Ebels, A.-L. Barra, A. Qaiumzadeh, A. Brataas, J. Sinova, and M. Kläui. Long-distance spin-transport across the Morin phase transition up to room temperature in ultra-low damping single crystals of the antiferromagnet  $\alpha\text{-Fe}_2\text{O}_3$ . *Nature Communications*, 11(1):6332, Dec 2020.
- <sup>10</sup>K. Grishunin, E. A. Mashkovich, A. V. Kimel, A. M. Balbashov, and A. K. Zvezdin. Excitation and detection of terahertz coherent spin waves in antiferromagnetic  $\alpha\text{-Fe}_2\text{O}_3$ . *Phys. Rev. B*, 104:024419, Jul 2021.
- <sup>11</sup>A. Ross, R. Lebrun, M. Evers, A. Deák, L. Szunyogh, U. Nowak, and M. Kläui. Exceptional sign changes of the nonlocal spin seebeck effect in antiferromagnetic hematite. *Phys. Rev. B*, 103:224433, Jun 2021.
- <sup>12</sup>M. Bialek, J. Zhang, H. Yu, and J.-Ph. Ansermet. Strong coupling of antiferromagnetic resonance with subterahertz cavity fields. *Phys. Rev. Applied*, 15:044018, Apr 2021.
- <sup>13</sup>I. Boverter, H. T. Simensen, B. Brekke, M. Weides, A. Anane, M. Kläui, A. Brataas, and R. Lebrun. Antiferromagnetic cavity magnon polaritons in collinear and canted phases of hematite, 2022.
- <sup>14</sup>Sh. G. Chou, P. E. Stutzman, Sh. Wang, E. J. Garboczi, W. F. Egelhoff, and D. F. Plusquellic. High-Resolution Terahertz Optical Absorption Study of the Antiferromagnetic Resonance Transition in Hematite ( $\alpha\text{-Fe}_2\text{O}_3$ ). *The Journal of Physical Chemistry C*, 116(30):16161–16166, 2012.
- <sup>15</sup>R. Przeniosło, I. Sosnowska, M. Stekiel, D. Wardecki, A. Fitch, and J. B. Jasiński. Monoclinic deformation of the crystal lattice of hematite  $\alpha\text{-Fe}_2\text{O}_3$ . *Physica B: Condensed Matter*, 449:72 – 76, 2014.
- <sup>16</sup>I. Dzyaloshinsky. A thermodynamic theory of “weak” ferromagnetism of antiferromagnetics. *Journal of Physics and Chemistry of Solids*, 4(4):241 – 255, 1958.
- <sup>17</sup>A. H. Morrish. *Antiferromagnetism*, chapter 8, pages 432–485. John Wiley & Sons, Ltd, 2001.
- <sup>18</sup>L. V. Velikov and E. G. Rudashevskii. Antiferromagnetic resonance in hematite in the weakly ferromagnetic state. *Soviet Physics JETP*, 29(5):836, May 1969.
- <sup>19</sup>I. Zavislyak and H. Chumak. Tunable reflective structures based on weak ferromagnetics and their application as tunable sub-terahertz resonators. *Radioelectronics and Communications Systems*, 62(8):377–390, Aug 2019.
- <sup>20</sup>B. R. Morrison, A. H. Morrish, and G. J. Troup. High-Field Antiferromagnetic Resonance in  $\alpha\text{-Fe}_2\text{O}_3$ . *physica status solidi (b)*, 56(1):183–195, 1973.
- <sup>21</sup>I. Boverter, H. T. Simensen, A. Anane, M. Kläui, A. Brataas, and R. Lebrun. Room-temperature antiferromagnetic resonance and inverse spin-hall voltage in canted antiferromagnets. *Phys. Rev. Lett.*, 126:187201, May 2021.
- <sup>22</sup>Hailong Wang, Yuxuan Xiao, Mingda Guo, Eric Lee-Wong, Gerald Q. Yan, Ran Cheng, and Chunhui Rita Du. Spin pumping of an easy-plane antiferromagnet enhanced by dzyaloshinskii-moriya interaction. *Phys. Rev. Lett.*, 127:117202, Sep 2021.
- <sup>23</sup>C. Caspers, V. P. Gandhi, A. Magrez, E. de Rijk, and J.-P. Ansermet. Sub-terahertz spectroscopy of magnetic resonance in  $\text{BiFeO}_3$  using a vector network analyzer. *Applied Physics Letters*, 108(24):241109, 2016.
- <sup>24</sup>M. Bialek, A. Magrez, A. Murk, and J.-Ph. Ansermet. Spin-wave resonances in bismuth orthoferrite at high temperatures. *Phys. Rev. B*, 97:054410, Feb 2018.
- <sup>25</sup>M. Bialek, T. Ito, H. Rønnow, and J.-Ph. Ansermet. Terahertz-optical properties of a bismuth ferrite single crystal. *Phys. Rev. B*, 99:064429, Feb 2019.
- <sup>26</sup>M. Bialek, A. Magrez, and J.-Ph. Ansermet. Spin-wave coupling to electromagnetic cavity fields in dysprosium ferrite. *Phys. Rev. B*, 101:024405, Jan 2020.
- <sup>27</sup>D. L. A. de Faria, S. Venâncio Silva, and M. T. de Oliveira. Raman microspectroscopy of some iron oxides and oxyhydroxides. *Journal of Raman Spectroscopy*, 28(11):873–878, 1997.
- <sup>28</sup>I. Chamrinski and G. Burns. Infrared- and raman-active phonons of magnetite, maghemite, and hematite: A computer simulation and spectroscopic study. *The Journal of Physical Chemistry B*, 109(11):4965–4968, 2005. PMID: 16863155.
- <sup>29</sup>A. M. Jubb and H. C. Allen. Vibrational spectroscopic characterization of hematite, maghemite, and magnetite thin films produced by vapor deposition. *ACS Applied Materials & Interfaces*, 2(10):2804–2812, 2010.
- <sup>30</sup>M. Eibschütz, S. Shtrikman, and D. Treves. Internal field in orthoferrites and the one third power law. *Solid State Communications*, 4(3):141 – 145, 1966.
- <sup>31</sup>S. G. Ovchinnikov, V. V. Rudenko, and V. I. Tugarinov. Temperature dependence of the uniaxial magnetic anisotropy of rhombohedral antiferromagnetic crystals with ions in the s state. *Physics of the Solid State*, 52(1):112–116, Jan 2010.
- <sup>32</sup>N. Pailhé, J. Majimel, S. Pechev, P. Gravereau, M. Gaudon, and A. Demourgues. Investigation of Nanocrystallized  $\alpha\text{-Fe}_2\text{O}_3$  Prepared by a Precipitation Process. *The Journal of Physical Chemistry C*, 112(49):19217–19223, 2008.